IJMMM International Journal of Minerals, Metallurgy and Materials 矿物冶金与材料学报（英文版）

Dielectric relaxation and conduction mechanism in Aurivillius ceramic $Bi_5Ti_3FeO_{15}$

Rasmita Jena, K. Chandrakanta, P. Pal, Md. F. Abdullah, S. D. Kaushik, and A.K. Singh

Cite this article as:
Rasmita Jena, K. Chandrakanta, P. Pal, Md. F. Abdullah, S. D. Kaushik, and A.K. Singh, Dielectric relaxation and conduction mechanism in Aurivillius ceramic $Bi_5Ti_3FeO_{15}$, *Int. J. Miner. Metall. Mater.*, 28(2021), No. 6, pp. 1063-1071. https://doi.org/10.1007/s12613-020-2091-3

View the article online at SpringerLink or IJMMM Webpage.

Articles you may be interested in

Hong-pan Liu, Xiao-feng Huang, Li-ping Ma, Dan-li Chen, Zhi-biao Shang, and Ming Jiang, Effect of Fe_2O_3 on the crystallization behavior of glass-ceramics produced from naturally cooled yellow phosphorus furnace slag, *Int. J. Miner. Metall. Mater.*, 24(2017), No. 3, pp. 316-323. https://doi.org/10.1007/s12613-017-1410-9

Tong-hua Liu, Wei Wang, Wen-jiang Qiang, and Guo-gang Shu, Mechanical properties and kinetics of thermally aged Z3CN20.09M cast duplex stainless steel, *Int. J. Miner. Metall. Mater.*, 25(2018), No. 10, pp. 1148-1155. https://doi.org/10.1007/s12613-018-1666-8

Sajjad Ali, Yaseen Iqbal, Inamullah Khan, Ansar Ullah, Muhammad Sadiq, Muhammad Fahad, and Khizar Hussain Shah, Hydrometallurgical leaching and kinetic modeling of low-grade manganese ore with banana peel in sulfuric acid, *Int. J. Miner. Metall. Mater.*, 28(2021), No. 2, pp. 193-200. https://doi.org/10.1007/s12613-020-2069-1

Lei Tian, Ao Gong, Xuan-gao Wu, Yan Liu, Zhi-feng Xu, and Ting-an Zhang, Cu^{2+}-catalyzed mechanism in oxygen-pressure acid leaching of artificial sphalerite, *Int. J. Miner. Metall. Mater.*, 27(2020), No. 7, pp. 910-923. https://doi.org/10.1007/s12613-019-1918-2

Sung Jin Kim, Kang Mook Ryu, and Min-suk Oh, Addition of cerium and yttrium to ferritic steel weld metal to improve hydrogen trapping efficiency, *Int. J. Miner. Metall. Mater.*, 24(2017), No. 4, pp. 415-422. https://doi.org/10.1007/s12613-017-1422-5

Mohamed Reda Boudchicha, Fausto Rubio, and Slimane Achour, Synthesis of glass ceramics from kaolin and dolomite mixture, *Int. J. Miner. Metall. Mater.*, 24(2017), No. 2, pp. 194-201. https://doi.org/10.1007/s12613-017-1395-4

IJMMM WeChat

QQ author group

International Journal of Minerals, Metallurgy and Materials
Volume 28, Number 6, June 2021, Page 1063
https://doi.org/10.1007/s12613-020-2091-3

Dielectric relaxation and conduction mechanism in Aurivillius ceramic $Bi_5Ti_3FeO_{15}$

Rasmita Jena[1)], *K. Chandrakanta*[1)], *P. Pal*[1)], *Md. F. Abdullah*[1)], *S. D. Kaushik*[2)], *and A.K. Singh*[1)]

1) Department of Physics and Astronomy, National Institute of Technology Rourkela, Rourkela- 769008, Odisha, India
2) UGC-DAE Consortium for Scientific Research Mumbai Centre, BARC, Mumbai- 400085, India
(Received: 11 January 2020; revised: 23 April 2020; accepted: 7 May 2020)

Abstract: For this study, we synthesized Aurivillius $Bi_5Ti_3FeO_{15}$ ceramic using the generic solid-state reaction route and then performed room-temperature X-ray diffraction to confirm that the compound had a single phase with no impurities. The surface morphology of the prepared sample was observed to contain microstructural grains approximately 0.2–2 μm in size. The dielectric properties of the sample were determined as a function of frequency in a range of approximately 100 Hz to 1 MHz at various temperatures (303 K ≤ T ≤ 773 K). Nyquist plots of the impedance data were found to exhibit a semi-circular arc in the high-temperature region, which is explained by the equivalent electrical circuit $(R_1C_1)(R_2QC_2)$, where R_1 and R_2 represent the resistances associated with the grains and grain boundaries, respectively, C_1 and C_2 are the respective capacitances, and Q is the constant phase element (CPE), which accounts for non-Debye type of behavior. Our results indicate that both the resistance and capacitance of the grain boundaries are more prominent than those of the grains. The alternating current (ac) conductivity data were analyzed based on the Jonscher universal power law, which indicated that the conduction process is dominated by the hopping mechanism. The calculated activation energies of the relaxation and conduction processes were very similar (0.32 to 0.53 eV), from which we conclude that the same type of charge carriers are involved in both processes.

Keywords: Nyquist plot; impedance spectroscopy; activation energy; ac conductivity; hopping

1. Introduction

The structure of the Aurivillius crystal was discovered by Aurivillius [1] in 1949 by his observations of the ferroelectricity in Bi_2WO_6. The crystal structure of Bi_2WO_6 consists of ABO_3 pervoskite blocks interlinked with Bi_2O_2 blocks. In the recent years, the layered structure of the Aurivillius family has attracted much attention because of its remarkable ferroelectric properties, low fatigue effects, and high Curie temperature (T_c) [2−4]. Various researchers have tailored its properties by inserting additional perovskite layers and controlling the concentration of magnetic/nonmagnetic ions at the magnetic sites. Among them, the bismuth-based Aurivillius compound $Bi_5Ti_3FeO_{15}$ (BTFO) is the most important due to its excellent ferroelectro-magnetic and highly flexible chemical properties [5−6]. Aurivillius-structured compounds have great potential for use in non-volatile random-access-memory applications, high-temperature pizeo-electrics, and photoluminescence [7−11]. The general expression for the Aurivillus compound is $(Bi_2O_2)^{2+}(A_{n-1}B_nO_{3n+1})^{2-}$, where A represents one of its 12 coordinated cations, including Na, Bi, K, Ca, Pb, Sr, Ba, and others; B represents the octahedral coordinated cations, e.g., Ti, Cr, Ta, Nb, and others; and n is the number of corners shared by the BO_6 octahedral sheets. This Aurivillius structure is composed of alternate stacks of fluorite-like $(Bi_2O_2)^{2+}$ and perovskite-like $(A_{n-1}B_nO_{3n+1})^{2-}$ layers oriented along the crystallographic c-axis [12−14]. For n = 4, the BTFO sample consists of an alternating sequence of $(Bi_3Ti_3FeO_{13})^{2-}$ and $(Bi_2O_2)^{2+}$ layers along the [001] direction.

An orthorhombic BTFO sample is reported to have an $A2_1am$ space group [15] with a ferroelectric transition temperature ~1003 K and an antiferromagnetic transition temperature (Néel temperature) of ~80 K [16−17]. The structural, magnetic, and transport properties of BTFO are highly dependent on the synthesis conditions. The electrical properties of this compound are reported to show significant variations with temperature, pressure, magnetic field, and frequency. To the best of knowledge, based on our literature review, few researchers have focused on the dielectric properties, relaxa-

Corresponding author: A.K. Singh E-mail: singhanil@nitrkl.ac.in

tion behavior, and conduction mechanisms of BTFO [18−20]. To better understand the microstructural behavior of its grains and grain boundaries, studies of their electrical properties are essential. The relaxation behavior in the material cannot be identified by dielectric measurement. Complex impedance spectroscopy (CIS), modulus analysis, and conductivity studies are promising techniques for characterizing the dielectric relaxation behavior. In addition, the alternating current (ac) conductivity can provide clear insight regarding the long-range hopping mechanism of the charge carriers [21−23].

In this study, our preparation of the $Bi_5Ti_3FeO_{15}$ sample was followed by the standard solid-state sintering process. The materials were subjected to comprehensive microstructure, dielectric, impedance, and modulus analyses. To understand the relaxation behavior, we fitted CIS, modulus, and conductivity plots using the electrical equivalent circuit $(R_1C_1)(R_2QC_2)$, theoretical Bergman modified KWW (Kohlraush–Williams–Watts) function, and Johnscher's single power law, respectively, where R_1 and R_2 represent the resistances associated with the grains and grain boundaries, respectively, C_1 and C_2 are the respective capacitances, and Q is the constant phase element (CPE), which accounts for non-Debye type of behavior. The analysis of conductivity data provides clear insight regarding the contribution of the direct current conductivity, the polarizability, and the strength of the interaction of mobile charge ions with neighboring lattices.

2. Experimental

The synthesis of the BTFO ceramic was followed by the conventional solid-state reaction process using high-purity oxide materials (>99.9%), i.e., Bi_2O_3, Ti_2O_3, and Fe_2O_3 (provided by Sigma-Aldrich). These oxides were used as precursors, weighted in desired proportions, and mixed thoroughly using an agate mortar and pestle in a stoichiometric ratio. This mixture was ground for 2 h, then pelletized and calcined at an optimized temperature of 800°C for 8 h in a Proportional-Integral-Derivative (PID) controlled programmable silicon-carbide tubular furnace. Then, the pre-treated pellets were again ground, pelletized, and finally sintered at 850°C for 8 h with a ramping rate of 4°C/min. The crystalline structure and phase of the material were then confirmed by X-ray diffraction (XRD) measurement at room temperature using a RIGAKU JAPAN and ULTIMA-IV diffractometer at Cu K_α radiation (λ = 0.15406 nm). The experimental data were obtained at a broad diffraction angle of 20° ≤ 2θ ≤ 60° with a step size of 0.02°/s and a scan rate of 3°/min. The microstructure of the BTFO sample was determined using a scanning electron microscopy (SEM) image via a JEOL/EO JSM-6480 LV system operating at an accelerating voltage of 30 kV. All the electrical measurements were made considering a parallel-plate capacitor configuration. The disk-shaped pellets of both sides were coated with silver paste, and ohmic contact was made using electrical probes. The frequency-dependent dielectric parameters, including the capacitance, dissipation factor, impedance, and phase factor, were characterized using a Wayne Kerr 6500B impedance analyzer with a drive ac voltage amplitude of 1 V over wide temperature (303 K ≤ T ≤ 773 K) and frequency (100 Hz ≤ f ≤ 1 MHz) ranges.

3. Results and discussion

3.1. XRD

XRD characterization analysis was performed to ensure the proper phase formation and to determine the crystal structure of the prepared sample. Fig. 1 shows the room-temperature XRD pattern of $Bi_5Ti_3FeO_{15}$, which reveals the formation of a single-phase material with no additional impurity phases. All the Bragg peaks are consistent with the standard JCPDS card no. (ICSD: 074037), which indicates an orthorhombic phase with space group $A2_1am$ [24]. To extract concise information about the structural parameters, we performed a Rietveld refinement of the experimental XRD data using FULLPROF Suite software by considering various parameters such as the background, zero shift, scale factor, atomic positions, thermal factors, lattice parameters, full width half maxima (FWHM), shape parameters, and preferred orientation. The peak shape parameters and background points were refined by considering the pseudo-Voigt function and performing a linear interpolation between a set of background points with refinable heights, respectively [25]. After a series of refinement cycles, the goodness of fit (χ^2) value is converged to 4.27. The lattice parameters obtained from the refinement are a = 0.54435 nm, b = 0.54652 nm, and c =

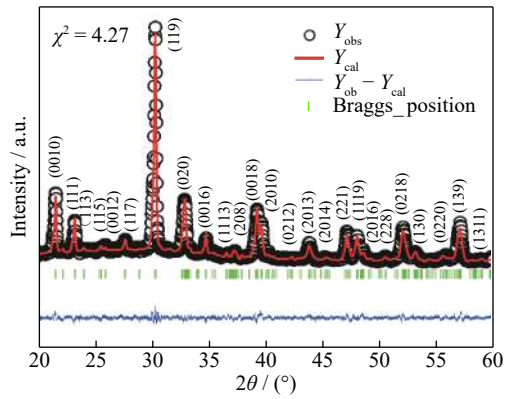

Fig. 1. Rietveld refinement of X-ray diffraction of orthorhombic BTFO sample observed at room temperature. The observed data points (Y_{obs}) shown in black hollow circles are well fitted with the calculated data points (Y_{cal}) represent in red line, but differences occur between the observed and calculated data ($Y_{obs} - Y_{cal}$), and Bragg reflections are represented by the blue and green lines.

4.13482 nm with cell volume V = 1.23012 nm^3. We estimated the goodness of fit (GOF) using GOF = R_{wp}/R_{exp}, where R_{wp} is the weighted pattern residual and R_{exp} is the expected residual, which was determined to be good (2.1). In addition, the highest intensity diffraction peak was found to correspond to a (119) orientation, which accords with the general formula for an Aurivillius compound (112n + 1) [26].

3.2. Morphological study by SEM

We determined the microstructural behavior of the BTFO from the SEM micrograph shown in Fig. 2(a), which indicates that the bulk BTFO consists of overlapping plate-like grains that have no microscopic defects such as cracks or micro cracks. The grains are not compactly packed, with the larger grains are separated from the smaller grains by the grain boundaries. The size of these nonhomogeneous plate-like grains varied from 0.2 to 2 μm and were distributed over the entire surface of the bulk material. Fig. 2(b) shows the energy dispersive X-ray (EDX) spectrum of the BTFO sample, which confirm that within the limit of experimental error, all the elements, i.e., Bi, Ti, Fe, and O, are present in the appropriate atomic percentages.

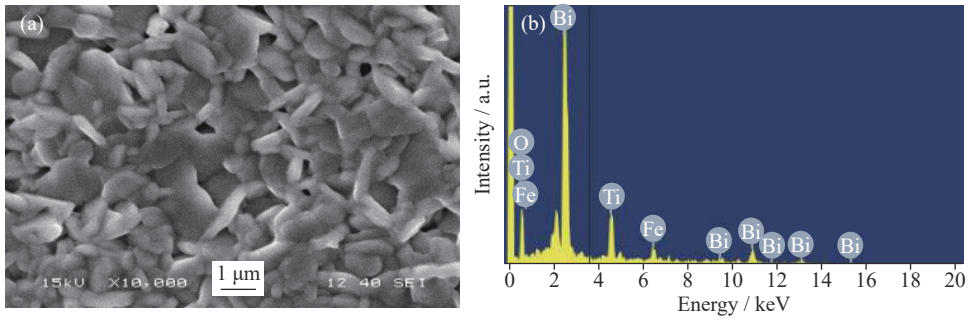

Fig. 2. (a) SEM micrograph and (b) EDX spectrum of BTFO sample.

3.3. Dielectric relaxation properties

Figs. 3(a) and 3(b) show the variation in the dielectric permittivity (ε') and loss spectra (tan δ) as a function of frequency over temperatures ranging from 303 to 773 K, respectively. The values of ε' and tan δ increase significantly with decreases in the frequency and increases in the temperature, and then stabilize with further increases in frequency. This is due to the contribution of both extrinsic and intrinsic polarizations. Extrinsic polarization arises because of the defects, dislocation of charge carriers, space charge polarization, and electrode interface (i.e. Maxwell Wagner effect), whereas intrinsic polarization arises due to the different kinds of polarization, i.e., electronic, ionic, and dipolar [27]. In the low-frequency regime, high dielectric dispersion is observed, which may be due to the extrinsic contribution. In Bi-based Aurivillius compounds, fluctuation in the valence states of different ions Fe^{2+}, Fe^{3+}, Ti^{3+}, and Ti^{4+} is also reported, which cause high dielectric dispersion. Fluctuation in the various valence states occurs due to the presence of Bi lone-pair electrons (6s) that diminish the oxygen percentage in the material. Fluctuations in the valence state cause electron hopping, which increases with increasing temperature. The gradual decrease of ε′ with increases in frequency is mainly due to the reduced dispersion of the space charges [28]. An increase in the leakage current at low frequency and high temperature results in high dielectric loss, which correlates with the results of our conductivity study.

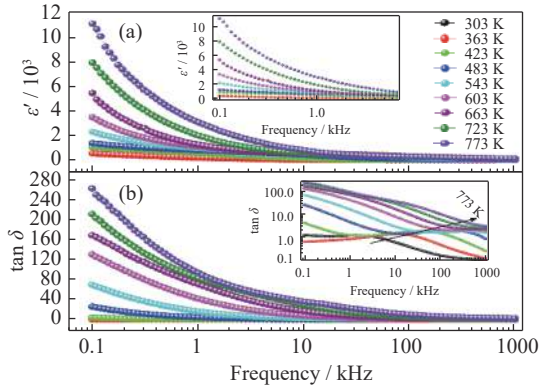

Fig. 3. (a) Variation in dielectric dispersion (ε') and (b) loss (tan δ) with frequency at different temperatures from 303 to 773 K. The inset images in (a) and (b) are the magnified view of dielectric dispersion (ε') and loss (tan δ) respectively.

3.4. Impedance spectroscopy

To investigate the different relaxation mechanisms that occur in the ceramic sample, we performed impedance spectroscopy to gain greater insight about the homogeneous and nonhomogeneous distributions of the grains and grain boundaries in the material. Various relaxation behaviors arise because of the contributions of the grains, grain boundaries, and electrode-interface phenomena. To gain a better understanding of the different relaxation mechanisms present in BTFO, we performed a Cole–Cole analysis [29]. Fig. 4(a) shows the complex impedance spectrum (Nyquist plot) of the impedance data, which plots the imaginary impedance (Z') versus the real impedance (Z') at different fixed temperatures.

To determine the correlation between the observed and experimental data, we fitted the experimental data (inset of Fig. 4) using an equivalent electrical circuit $(R_1C_1)(R_2QC_2)$ and ZSIMP WIN software (version 3.21). The mathematical relation of the CPE impedance is given as follows [2]:

$$Z_{\mathrm{CPE}} = \frac{1}{[B(\mathrm{j}\omega)^n]} \tag{1}$$

where B, j, ω, and n $(0 \le n \le 1)$ are the pre-exponential factor, imaginary factor of value $\sqrt{-1}$, angular frequency, and empirical exponent, respectively. For $n = 1$, the CPE is regarded as an ideal capacitor, whereas $n = 0$ corresponds to the actual resistance [30]. As above, the fitted impedance parameters R_1 and R_2 are the respective resistances of the grain and grain boundaries at different temperatures, which are summarized in Table 1. In the low-temperature regime (below 400 K), the Cole–Cole plots resemble incomplete semi-circular arcs (303 and 363 K) for low Z' values. For high Z' values, we observe nearly straight lines with steep slopes, which indicates the strong insulating nature of the sample. With gradual increases in temperature, the straight line bends towards the real impedance (Z') and forms a distorted semi-circular arc. Further increases in the temperature causes the center of the

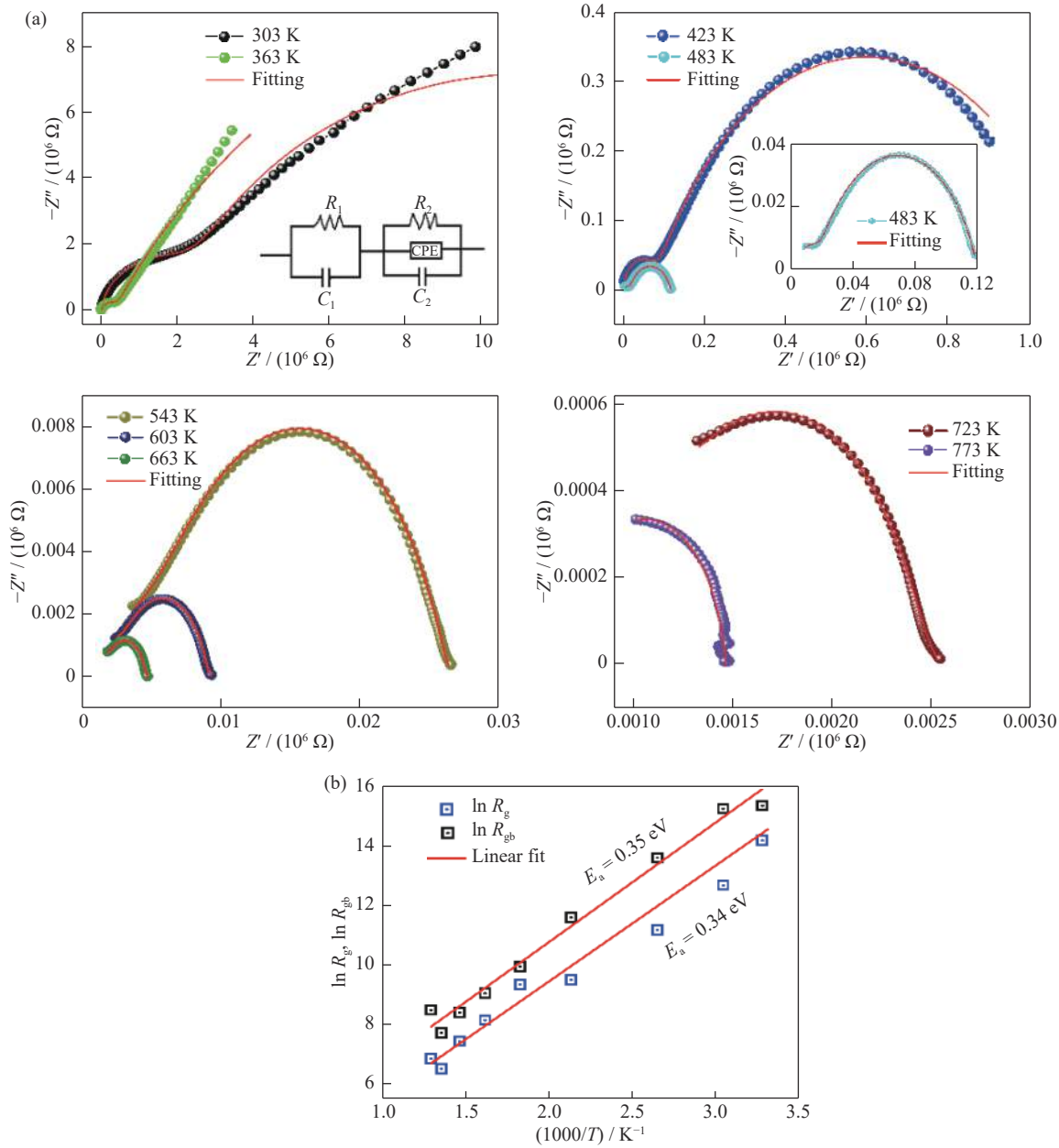

Fig. 4. (a) Cole–Cole or Nyquist plot of BTFO sample at fixed various temperatures, and fitted with an equivalent circuit (inset). (b) Activation energies of both the grains and grain boundaries calculated from the plot of the linear fit (solid red line) of the logarithmic R_g and R_{gb} versus 1000/T.

semi-circular arcs to shift to the complex impedance origin. Eventually, the maxima and diameter of the respective semi-circular arcs decrease, which indicates a pronounced increase in the direct current (dc) conductivity in the samples [31]. The results obtained from the fitted impedance data indicate that the resistance of the grain boundaries (R_2) is greater than that of the grains (R_1), so the gross resistance in the material is primarily due to the contribution of the grain boundaries. Both resistances R_1 and R_2 are observed to decrease with increases in temperature, which indicates a negative temperature coefficient of resistance (NTCR), i.e., semiconducting behavior by the sample [32]. We calculated the activation energies of R_1 and R_2 from the Arrhenius plot, as shown in Fig. 4(b), which reveals that the activation energy of R_2 (= R_{gb}) (E_a = 0.35 eV) is larger than that of R_1 (= R_g) (E_a = 0.34 eV).

Table 1. Resistances of grains (R_1) and grain boundaries (R_2) at various temperatures, obtained by fitting the semi-circular arcs of the impedance with the electrical equivalent circuit

T / K	R_1 / (10^4 Ω)	R_2 / (10^4 Ω)	CPE	
			B	n
303	143.6	452.5	1.70×10^{-9}	0.57
363	31.37	474.4	2.54×10^{-9}	0.64
423	7.009	107.7	4.02×10^{-9}	0.80
483	1.329	10.93	5.41×10^{-9}	0.80
543	1.137	1.609	2.93×10^{-5}	0.41
603	0.344	0.599	2.51×10^{-11}	0.43
663	0.169	0.303	8.00×10^{-9}	0.80
723	0.068	0.187	1.83×10^{-4}	0.47
773	0.095	0.481	1.56×10^{-3}	0.80

3.5. Modulus analysis

The electric modulus formalism distinguishes between microscopic processes, which are associated with conduction mechanisms, and localized dielectric relaxations. As the impedance is obtained from the resistance of the sample in the same way, the modulus is dictated by the inverse permittivity of the sample. The mathematical relation of a complex modulus (M^*) in terms of impedance is expressed as follows:

$$M^* = \frac{1}{\epsilon^*} = \mathrm{j}\omega c_0 Z^* \tag{2}$$

$$M^* = M' + \mathrm{j}M'' = \mathrm{j}\omega c_0 (Z' - \mathrm{j}Z'') \tag{3}$$

Thus, the real (M') and imaginary (M'') parts of the complex modulus are written as follows:

$M' = \omega c_0 Z''$,

$M'' = \omega c_0 Z'$,

where Z', Z'', ω (= $2\pi f$), and c_0 (= $\epsilon_0 A/d$, where ϵ_0 is the free space permittivity, A is the surface area, and d is thickness of the sample) are the real and imaginary parts of the modulus, the angular frequency, and the free-space capacitance, respectively. Figs. 5(a) and 5(b) show the difference between the M' and M'' moduli with respect to frequency for a large frequency range and a fixed temperature range from 303 to 773 K. We note that the maxima of M' are displaced to the high-frequency regime with increases in temperature and most of the peaks are no longer in the frequency window on the right side. In the low-frequency region, the value of M' is very low, nearly equal to zero, but it increases with increases in frequency. This conduction mechanism is due to the characteristic short-range mobility of the charge carriers. The M'' versus frequency plot indicates that with increases in temperature the relaxation peaks migrate to the higher-frequency region. The frequency region below the maximum peak determines the range in which charge carriers are mobile over long distances. At high frequencies above the highest peak, the charge carriers are confined to the potential well, and are mobile only over short distances [33]. This behavior of the modulus spectra suggest that the activation process is thermally activated, with long-range hopping taking place at high temperature. We fitted the experimental data of M'' using the theoretical modified Bergman KWW (Kohlraush–Williams–Watts) function [34], with the imaginary modulus given by the following:

$$M'' = \frac{M''_{\max}}{\left\{1 - \beta + (\beta/1+\beta)\left[\beta(\omega_{\max}/\omega) + (\omega/\omega_{\max})\right]^{\beta}\right\}} \tag{4}$$

where $M''_{\max}$ is the maximum value of the imaginary modulus, $\omega_{\max}$ is the maximum angular frequency of the respective modulus, and β is the exponent that denotes deviation from the ideal Debye type of behavior, which is related to the FWHM of the M'' versus frequency curve. We obtained the values of β from the fitted data. The inset in Fig. 4(b) shows the variation of β at different temperatures, which indicates that β = 1 corresponds to the ideal Debye type of behavior with a distinct relaxation time, whereas β = 0 indicates the highest number of dipolar interactions. Fig. 5(c) shows the scaling behavior of the sample, with a plot of the normalized modulus $M''/M''_{\max}$ versus normalized frequency $f/f''_{\max}$ at selected temperatures, i.e., 303, 363, 423, and 483 K. This plot reveals that almost all the peaks collapse into one master curve at different temperatures and that the dynamic processes are temperature-independent in the low-frequency region. It is interesting to note that with an increase in frequency, a transition from long-range to short-range motion occurs. Fig. 5(d) shows $\ln\tau^m$ versus 1000/T, from which the dielectric relaxation time (τ^m) can be derived by the relation $\tau^m = 1/\omega^m = 2\pi f^m$, where ω^m is the maximum angular frequency and f^m is the maximum frequency at the highest value of M''. The dynamics of the relaxation process can be analyzed using the Arrhenius law, which is expressed in terms of the relaxation time τ^m as $\tau^m = \tau_0 \exp(E_a/k_B T)$ [35]. Here, τ_0, E_a, k_B, and T are the pre-exponential factor, the activation energy of the charge carriers, the Boltzmann con-

stant, and the absolute temperature, respectively. We extracted the activation energy (E_a = 0.32 eV) of the modulus from the linear fitting of the Arrhenius plot, from which we found that the activation energies of the impedance and modulus are comparable at 0.35 and 0.32 eV, which indicates that the same type of charge carriers participate in both the relaxation and conduction processes [36].

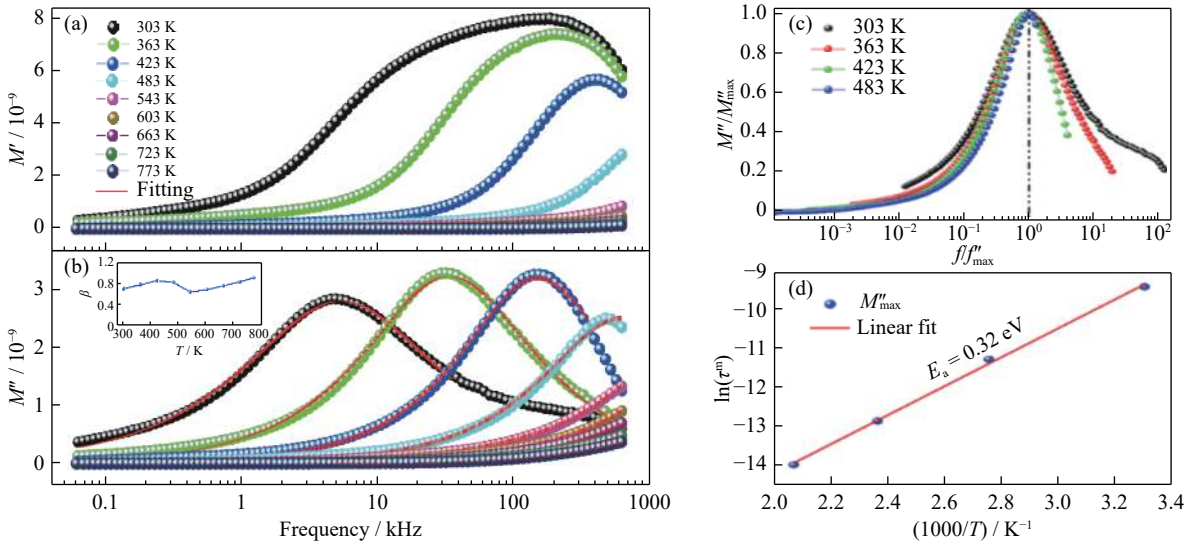

Fig. 5. Temperature dependence of (a) real and (b) imaginary moduli as a function of frequency, inset: variation of β with temperature. (c) Scaling behavior of imaginary modulus with frequency at selected temperatures (303, 363, 423, and 483 K). (d) Relaxation properties of BTFO sample obtained from the maxima of the imaginary modulus.

3.6. Electrical conductivity analysis

Electrical conductivity in the material is a thermally activated process in which bound charge carriers move in an orderly manner with the application of an external electric field. One of the crucial properties of the material is the characteristic behavior of its charge carriers. Fig. 6(a) shows a plot of the ac conductivity (σ_{ac}) versus frequency in a selected temperature range of 483 to 773 K. Eq. (5) provides the ac conductivity in terms of empirical impedance [37]:

$$\sigma_{ac} = \frac{Z' \times t}{A\left[(Z')^2 + (Z'')^2\right]} \tag{5}$$

where A and t correspond to the respective surface area and thickness of the sample. The conductivity plot has the following set of characteristics: (1) We observed plateau-like behavior in the low-frequency region, which is due to the long-range translational motion of ions in the direct current conductivity σ_{dc} region. We also found conductivity σ_{dc} to increase with increases in temperature, which indicates that the electrical conductivity of the material is mainly due to a thermally activated process. (2) In the high-frequency region, conductivity was found to depend on the $A\omega^n$ of Johnscher's power law, which is given as [38]:

$$\sigma(\omega) = \sigma_{dc} + A\omega^n \tag{6}$$

where $\sigma(\omega)$ is the total conductivity, i.e., the sum of the ac and dc conductivities of the material, σ_{dc} is the direct current conductivity, $A\omega^n$ is the pure dispersive term of the ac conductivity, A is the pre-exponential factor that determines the strength of the polarizability, ω (= $2\pi f$) is the angular frequency, and n is the exponent ($0 \le n \le 1$), which indicates the degree of interaction between the mobile charge ions with the surrounding lattice. According to the Johnscher power law, frequency-dispersion conductivity occurs because of the relaxation of the ionic atmosphere arising from the mobile charge carriers [39]. Using Eq. (6), the experimental conductivity plot is well fitted up to the high-frequency range (~10^5 Hz) and found to obey the Jonscher power law over the all temperatures range. Table 2 lists the fitted parameters of the ac conductivities. The inset in Fig. 6(a) shows that exponents n and A are obtained from the fitted data as a function of temperature. The values of n indicate the motion of the charge carriers, i.e., translational motion and localization. If $n < 1$, the motion of the charge carrier is translational, and if $n > 1$, the motion is localized. We determined that the value of n increases with increases in temperature to approximately 663 K, but then decreases up to 773 K. This indicates that hopping conduction by the charge carriers occurs in the sample. In the literature, different hopping mechanisms are reported to occur at different temperatures and frequencies; the increases in the values of n with increasing temperature indicate small polaron hopping whereas decreases in the values of n with increases in temperature indicate large polaron hopping [40]. Fig. 6(b) shows the variation in dc conductivity with inverse temperature, in which we can observe that σ_{dc} increases with increases in temperature, and follows the

thermally activated Arrhenius type of relation:

$$\sigma_{dc} = \sigma_0 \exp\left(\frac{-E_a}{k_B T}\right) \quad (7)$$

where σ_0, E_a, k_B, and T are the pre-exponential factor, activation energy, Boltzmann constant, and absolute temperature, respectively [41]. From the slope of the linear fitting of the dc conductivity data, we obtained an activation energy of approximately 0.53 eV. Thus, all the extracted activation energies of the BTFO material lie within the range of 0.32 to 0.53 eV. This result indicates that the long-range hopping of polarons is responsible for the electrical conductivity in the material. Eventually, the activation energies calculated for both the relaxation and electrical conduction processes become very similar, which confirms that the dielectric relaxation and conduction processes have the same type of charge carriers.

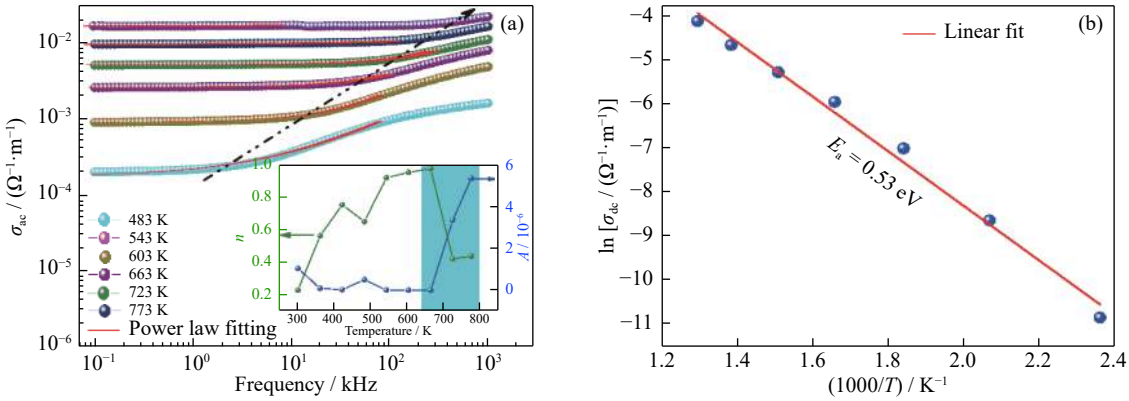

Fig. 6. (a) Temperature-dependent ac conductivity (σ_{ac}) versus frequency in the range of 483 to 773 K. The solid lines (red) represent the fit of Johnscher's power law. The inset figure is the variation of the fitting parameters (*n*, *A*) with temperature. (b) Logarithmic dc conductivity (σ_{dc}) versus inverse temperature of the BTFO ceramic, with the solid red line showing the linear fit of the data.

Table 2. Various parameter values for *A* and *n* of ac conductivity at selected temperatures

Temperature / K	*A*	*n*
483	4.96×10^{-7}	0.647
543	6.75×10^{-9}	0.915
603	3.95×10^{-9}	0.947
663	2.30×10^{-9}	0.970
723	3.33×10^{-6}	0.420
773	5.31×10^{-9}	0.435

4. Conclusion

In this work, we synthesized a single-phase $Bi_5Ti_3FeO_{15}$ sample using the generic solid-state sintering method, with our analysis of the room-temperature XRD data indicating that the BTFO material had an orthorhombic crystal structure with the space group $A2_1am$. The SEM and EDX spectra confirmed the growth in the grain size and the presence of all the appropriate constituents in the sample, respectively. The electrical properties of the BTFO ceramic, obtained over wide temperature and frequency ranges, revealed NTCR behavior. Our impedance analysis confirmed the primary contribution of the grain boundaries to the electrical properties, with the resistance and capacitance of the grain boundaries more prominent than that of the grains. We also showed that the both the grains and grain boundaries exhibit non-Debye relaxation behavior. The electrical conductivity spectra were found to obey the Jonscher universal power law over the entire temperature range. The significant decrease in exponent *n* above 663 K suggests the involvement of two kinds of hopping mechanisms in the BTFO ceramic. Below 663 K, a long-range hopping mechanism is present, whereas above 663 K, a neighboring-site hopping mechanism is evident. Lastly, the activation energies (E_a) extracted from the impedance, modulus, and dc conductivity analyses were very similar ($0.32\ \text{eV} \le E_a \le 0.53\ \text{eV}$), which reveals that the same kind of charge carriers are responsible for both the dielectric relaxation and electrical conductivity processes in the sample.

Acknowledgements

Anil Kumar Singh acknowledges the Board of Research in Nuclear Science (BRNS), Mumbai (Sanction No. 2012/37P/40/BRNS/2145), the UGC-DAE Consortium for Scientific Research, Mumbai (Sanction No. CRS-M-187, 225), and the Science and Engineering Research Board (SERB), New Delhi (Sanction No. SR/FTS/PS-187/2011) for funding.

References

[1] B. Aurivillius, Mixed bismuth oxides with layer lattices, *I. Ark. Kemi*, 1(1949), p. 463.
[2] Y.L. Bai, B. Yang, and S.F. Zhao, *In-situ* stress modulated ferroelectric photovoltaic effect in cluster-assembled $TbFe_2/Bi_5Ti_3FeO_{15}$ heterostructural films, *Appl. Phys. Lett.*, 115(2019), No. 26, p. 261602.
[3] C. A-Paz de Araujo, J.D. Cuchiaro, L.D. McMillan, M.C. Scott, and J.F. Scott, Fatigue-free ferroelectric capacitors with platinum electrodes, *Nature*, 374(1995), No. 6523, p. 627.
[4] B.H. Park, B.S. Kang, S.D. Bu, T.W. Noh, J. Lee, and W. Jo, Lanthanum-substituted bismuth titanate for use in non-volatile memories, *Nature*, 401(1999), No. 6754, p. 682.
[5] A. Birenbaum and C. Ederer, Potentially multiferroic Aurivillius phase $Bi_5Ti_3FeO_{15}$: Cation site preference, electric polarization and magnetic coupling from first principles, *Phys. Rev. B*, 90(2014), No. 21, art. No. 214190.
[6] F.J. Geng, C.H. Yang, C. Feng, P.P. Lv, X.M. Jiang, Q. Yao, Q. Zhang, C. Wei, and P. Song, Effects of single-coated layer thickness on the microstructure, leakage current and dielectric tenability of $Na_{0.5}Bi_{0.5}$(Ti, Zn) $O_{3-\delta}$ thin films prepared by metal organic decomposition, *J. Alloys. Compd.*, 663(2016), p. 659.
[7] E.C. Subarao, Crystal chemistry of mixed bismuth oxides with layer-type structure, *J. Am. Ceram. Soc.*, 45(1962), No. 4, p. 166.
[8] Y.L. Bai, J.Y. Chen, X. Wu, and S.F. Zhao, Photovoltaic behaviors regulated by band-gap and bipolar electrical cycling in holmium-doped $Bi_5Ti_3FeO_{15}$ ferroelectric films, *J. Phys. Chem. C*, 120(2016), No. 43, p. 24637.
[9] H. Ogawa, M. Kimura, A. Ando, and Y. Sakabe, Temperature dependence of piezoelectric properties of grain oriented $CaBi_4Ti_4O_{15}$ ceramics, *Jpn. J. Appl. Phys.*, 40(2001), p. 5715.
[10] S. Ida, C. Ogata, U. Unal, K. Izawa, T. Inoue, O. Altuntasoglu, and Y. Matsumoto, Preparation of a blue luminescent nanosheet derived from layered perovskite $Bi_2SrTa_2O_9$, *J. Am. Chem. Soc.*, 129(2007), No. 29, p. 8956.
[11] C.B. Long, H.Q. Fan, and P.R. Ren, Structure, phase transition behaviors and electrical properties of Nd substituted Aurivillius ploycrystallines $Na_{0.5}Nd_x$ $Bi_{2.5-x}$ Nb_2O_9 (x = 0.1, 0.2, 0.3, and 0.5), *Inorg. Chem.*, 52(2013), No. 9, p. 5045.
[12] R.E. Newnham, R.W. Wolfe, and J.F. Dorrian, Structural basis of ferroelectricity in the bismuth titanate family, *Mater. Res. Bull.*, 6(1971), No. 10, p. 1029.
[13] Z.H. Tang, B. Yang, J.Y. Chen, Q.S. Lu, and S.F. Zhao, Strong magnetoelectric coupling of Aurivillius phase multiferroic composite films with similar layered perovskite structure, *J. Alloys. Compd.*, 772(2019), p. 298.
[14] E.C. Subbarao, A family of ferroelectric bismuth compounds, *J. Phys. Chem. Solids*, 23(1962), No. 6, p. 665.
[15] C.H. Hervoches, A. Snedden, R. Riggs, S.H. Kilcoyne, P. Manuel, and P. Lightfoot, Structural behaviour of the four-layer aurivillius-phase ferroelectrics, *J. Solid State Chem.*, 164(2002), No. 2, p. 280.
[16] X.W. Dong, K.F. Wang, J.G. Wan, J.S. Zhu, and J.M. Liu, Magnetocapacitance of polycrystalline $Bi_5Ti_3FeO_{15}$ prepared by sol−gel method, *J. Appl. Phys.*, 103(2008), No. 9, art. No. 094101.
[17] A. Srinivas, S.V. Suryanarayan, G.S. Kumar, and M.M. Kumar, Magnetoelectric measurements on $Bi_5Ti_3FeO_{15}$ and $Bi_6Fe_2TiO_{18}$, *J. Phys. Condens. Matter*, 11(1999), p. 3335.
[18] A. Mohapatra, P.R. Das, and R.N.P. Choudhary, Structural and electrical properties of $Bi_5Ti_3FeO_{15}$ ceramics, *J. Mater. Sci. Mater. Electron.*, 25(2014), No. 3, p. 1348.
[19] N.S. Zhao, H.Q. Fan, X.H. Ren, J.W. Ma, J. Bao, Y.J. Guo, and Y.Y. Zhou, Dielectric, impedance and piezoelectric properties of $(K_{0.5}Nd_{0.5})TiO_3$-doped $0.67BiFeO_3$−$0.33BaTiO_3$ ceramics, *J. Eur. Ceram. Soc.*, 39(2019), No. 14, p. 4096.
[20] B.B. Yan, H.Q. Fan, C. Wang, M.C. Zhang, A.K. Yadav, X.K. Zheng, H. Wang, and Z.N. Du, Giant electro-strain and enhanced energy storage performance of $(Y_{0.5}Ta_{0.5})^{4+}$ co-doped $0.94(Bi_{0.5}Na_{0.5})TiO_3$−$0.06BaTiO_3$ lead-free ceramics, *Ceram. Int.*, 46(2020), No. 1, p. 281.
[21] C. Ang, Z. Yu, Z. Jing, P. Lunkenheimer, and A. Loidl, Dielectric spectra and electrical conduction in Fe-doped $SrTiO_3$, *Phys. Rev. B*, 61(2002), No. 6, p. 3922.
[22] G.Z. Dong, H.Q. Fan, H.L. Tian, J.W. Fang, and Q. Li, Gas-sensing and electrical properties of perovskite structure p-type barium-substituted bismuth ferrite, *RSC Adv.*, 5(2015), No. 38, p. 29618.
[23] Y.W. Zhao, H.Q. Fan, K. Fu, L.T. Ma, M.M. Li, and J.W. Fang, Intrinsic electric field assisted polymeric graphitic carbon nitride coupled with $Bi_4Ti_3O_{12}/Bi_2Ti_2O_7$ heterostructure nanofibers toward enhanced photocatalytic hydrogen evolution, *Int. J. Hydrogen Energy*, 41(2016), No. 38, p. 16913.
[24] X.Y. Mao, W. Wang, and X.B. Chen, Electrical and magnetic properties of $Bi_5Ti_3FeO_{15}$ compound prepared by inserting $BiFeO_3$ into $Bi_4Ti_3O_{12}$, *Solid State Commun.*, 147(2008), No. 5-6, p. 186.
[25] H.M. Rietveld, A profile refinement method for nuclear and magnetic structures, *J. Appl. Cryst.*, 2(1969), No. 2, p. 65.
[26] Z.H. Peng, D.X. Yan, Q. Chen, D.Q. Xin, D.Q. Liu, D.Q. Xiao, and J.G. Zhu, Crystal structure, dielectric and piezoelectric properties of Ta/W codoped Bi_3TiNbO_9 Auriviliius phase ceramics, *Curr. Appl. Phys.*, 14(2014), No. 12, p. 1861.
[27] Y. Zhu and A. Chen, Maxwell-Wagner polarization in ceramic composites $BaTiO_3$−$Ni_{0.3}Zn_{0.7}Fe_{2.1}O_4$, *J. Appl. Phys.*, 91(2002), No. 2, p. 794.
[28] S. Sen and R.N.P. Choudhary, Impedance studies of Sr modified $BaZr_{0.05}Ti_{0.95}O_3$ ceramics, *Mater. Chem. Phys.*, 87(2004), No. 2-3, p. 256.
[29] K.S. Cole and R.H. Cole, Dispersion and absorption in dielectrics I. alternating current characteristics, *J. Chem. Phys.*, 9(1941), No. 4, p. 341.
[30] F. Rehman, J.B. Li, J.S. Zhang, M. Rizwan, C. Niu, and H.B. Jin, Grains and grain boundaries contribution to dielectric relaxations and conduction of $Bi_5Ti_3FeO_{15}$ ceramics, *J. Appl. Phys.*, 118(2015), No. 21, art. No. 214101.
[31] A.K. Biswal, J. Ray, P.D. Babu, V. Siruguri and P.N. Vishwakarma, Dielectric relaxations in La_2NiMnO_6 with signatures of Griffths phase, *J. Appl. Phys.*, 115(2014), No. 19, p. 194106.
[32] A. Benali, M. Bejar, E. Dhahri, M.F.P. Graça, and L.C. Costa, Electrical conductivity and ac dielectric properties of $La_{0.8}Ca_{0.2-x}Pb_xFeO_3$ (x = 0.05, 0.10 and 0.15) perovskite compounds, *J. Alloys Compd.*, 653(2015), p. 506.
[33] A.H. Dhahri, E. Dhahri, and E.K. Hlil, Electrical conductivity and dielectric behaviour of nanocrystalline $La_{0.6}Gd_{0.1}Sr_{0.3}Mn_{0.75}Si_{0.25}O_3$, *RSC Adv.*, 8(2018), No. 17, p. 9103.
[34] T. Badapanda, S. Sarangi, S. Parida, B. Behera, B. Ojha, and S. Anwar, Frequency and temperature dependence dielectric study of strontium modified Barium Zirconium Titanate ceramics obtained by mechanochemical synthesis, *J. Mater. Sci. Mater. Electron.*, 26(2015), No. 5, p. 3069.
[35] D.C. Sinclair and A.R. West, Impedance and modulus spectroscopy of semiconducting $BaTiO_3$ showing positive temperature coefficient of resistance, *J. Appl. Phys.*, 66(1989), No. 8, p. 3850.

[36] R.J. Tang, C. Jiang, W.H. Qian, J. Jian, X. Zhang, H.Y. Wang, and H. Yang, Dielectric relaxation, resonance, and scaling behaviors in $Sr_3Co_2Fe_{24}O_{41}$ hexaferrite, *Sci. Rep.*, 5(2015), art. No. 13645.

[37] M.M. Hoque, A. Dutta, S. Kumar, and T.P. Sinha, Dielectric relaxation and conductivity of Ba $(Mg_{1/3}Ta_{2/3})$ O_3 and Ba $(Zn_{1/3}Ta_{2/3})$ O_3, *J. Mater. Sci. Technol.*, 30(2014), No. 4, p. 311.

[38] K. Funke, Jump relaxation in solid electrolytes, *Prog. Solid State Chem.*, 22(1993), No. 2, p. 111.

[39] E. Barsoukov and J.R. Macdonald, *Impedance Spectroscopy Theory, Experiment and Applications*, 2nd Ed., Wiley Interscience, New York, 2005, p. 14.

[40] N. Ortega, A. Kumar, P. Bhattacharya, S.B. Majumdar, and R.S. Katiyar, Impedance spectroscopy of multiferroic $PbZn_xTi_{1-x}O_3/CoFe_2O_4$ layered thin films, *Phys. Rev. B*, 77(2008), No. 1, art. No. 014111.

[41] A.K. Jonscher, The 'universal' dielectric response, *Nature*, 267(1977), No. 5613, p. 673.